Reference to published article:
Das, S., Lindsay, M.B.J., & Hendry, M.J. (2019). Selenate removal by zero-valent iron under anoxic conditions: Effects of nitrate and sulfate. *Environmental Earth Sciences* 78: 528. https://doi.org/10.1007/s12665-019-8538-z

Selenate removal by zero-valent iron under anoxic conditions: effects of nitrate and sulfate

Soumya Das*, Matthew B. J. Lindsay, M. Jim Hendry

Department of Geological Sciences, University of Saskatchewan, Saskatoon, Saskatchewan, Canada S7N 5E2

* Corresponding author: Tel: +1 306-966-4664; fax: +1-306-966-8593.

E-mail address: sod671@campus.usask.ca (S. Das).

Keywords: zero-valent iron, selenate, removal, reduction, sulfate, nitrate

ABSTRACT

Batch experiments were conducted to examine aqueous Se(VI) removal by zero-valent iron (ZVI) under anoxic conditions in the presence and absence of NO_3^- and SO_4^{2-}. Initial concentrations for Se(VI), SO_4 and NO_3–N of 5 mg L^{-1}, 1800 mg L^{-1} and 13 mg L^{-1}, respectively, were employed to mimic mine wasters. In the control experiment, 90% Se(VI) removal occurred within 1.5 h without SO_4^{2-} and NO_3^- (B1). This removal threshold was reached after 3 h with NO_3^- added (B3) and after 33 h with SO_4^{2-} added (B2). Removal reached 90% after 42 h with both SO_4^{2-} and NO_3^- added (B4). Modeled Se(VI) removal rates consistently followed first-order kinetics and revealed that the presence of SO_4^{2-} and, to a lesser extent, NO_3^- inhibited Se(VI) removal. Increases in pH and Fe coupled with decreasing Eh are consistent with ZVI corrosion under anoxic conditions. Transmission electron microscopy, Raman spectroscopy, and X-ray diffraction revealed magnetite [Fe_3O_4] and lepidocrocite [γ-FeOOH] formed at ZVI surfaces during the experiments. X-ray absorption near edge structure spectroscopy indicated that Se(VI) was predominantly reduced to Se(0) (70−80%), but Se(IV) (10−13%) and Se(-II) (2−13%) were also detected at reacted ZVI surfaces. Overall, the results show that although SO_4^{2-} and NO_3^- present in mine wastes can reduce reaction rates, Se(VI) removal by ZVI under anoxic conditions is associated with extensive reduction to insoluble Se(0).

INTRODUCTION

Selenium contamination of water resources by anthropogenic activities is a global environmental issue (Lemly, 2004). In particular, mining, metallurgy, and agriculture and petrochemical activities can increase concentrations of this potentially toxic element in ground and surface waters (Lemly, 2004; Palmer et al., 2010; Wellen et al., 2015). Mine wastes commonly contain sulfide minerals including pyrite [FeS_2], chalcopyrite [$CuFeS_2$] and sphalerite [ZnS] (Hendry et al., 2015; Riley et al., 2007; Yudovich and Ketris, 2006). Selenium substitutes for sulfur in these and other sulfide minerals (Diehl et al., 2012; Hendry et al., 2015; Kolker, 2012; Lussier et al., 2003), which can release sulfate and Se to surface and ground waters during oxidative dissolution (Essilfie-Dughan et al., 2017; Lindsay et al., 2015). This issue is particularly problematic in drainage from waste rock deposits at coal-mining operations (Hendry et al., 2015; Lussier et al., 2003). Elevated nitrate concentrations, which are derived from blasting agents, can also occur in drainage from waste rock at coal and other mining operations (Bailey et al., 2013; Hendry et al., 2018; Mahmood et al., 2017). Consequently, co-occurrence of Se with both SO_4^{2-} and NO_3^- is common in mining-impacted waters (Hendry et al., 2018; Essilfie-Dughan et al., 2017; Lindsay et al., 2015; Mahmood et al., 2017). Cost-effective techniques for Se removal are, therefore, needed to mitigate long-term environmental impacts of mining operations (Ziemkiewicz et al., 2011).

Selenium solubility and mobility is strongly dependent upon oxidation state and environmental factors including pH and redox setting (Yoon et al., 2011). Environmental mobility of Se generally increases with oxidation; Se(VI) oxyanions exhibit greater mobility than Se(IV) oxyanions, which exhibit greater tendency for sorption onto minerals and organics (Masscheleyn et al., 1990; Scheinost and Charlet, 2008; Tokunaga et al., 1997). Additionally, Se(0) and Se(−II)

are sparingly soluble and tend to form solids (Scheinost and Charlet, 2008; Masscheleyn et al., 1990; Tokunaga et al., 1997; Yoon et al., 2011). Therefore, Se removal can be achieved using various reactive materials that promote sorption reactions, reduction reactions, or both (Sasaki et al., 2008; Yigit and Tozum, 2012; Yoon et al., 2011). Previous studies have examined Se immobilization by various minerals, including iron (oxyhydr)oxides and manganese oxide (Balistrieri and Chao, 1990; Kang et al., 2002; Manceau and Charlet, 1994; Su and Suarez, 2000; Zhang and Sparks, 1990), and other reactive materials such as mixtures of zero valent iron and organic carbon (Sasaki et al., 2008; Gibson et al., 2012), pumice and volcanic slags (Yigit and Tozum, 2012) under a range of environmental conditions. However, zero-valent iron (ZVI) has proven particularly effective for passive treatment of Se(VI)-bearing waters (Gibson et al., 2012; Olegario et al., 2010; Tang et al., 2014; Yoon et al., 2011; Zhang et al., 2005).

Selenium removal by ZVI is achieved under both oxic and anoxic conditions via adsorption, reduction or a combination of these processes (Das et al., 2017; Gibson et al., 2012; Liang et al., 2015; Olegario et al., 2010; Shrimpton et al., 2015; Tang et al., 2014; Yoon et al., 2011; Zhang et al., 2005). More specifically, Se(VI) is reduced to Se(IV), which then adsorbs onto surface precipitates, including Fe (oxyhydr)oxides, at the reacted ZVI surface (Das et al., 2017; Gibson et al., 2012; Yoon et al., 2011). Following sorption, Se(IV) can be reduced to sparingly soluble Se(0) or Se(−II) phases (Gibson et al., 2012; Liang et al., 2013; Yoon et al., 2011; Yoon et al., 2016) Consequently, ZVI from different sources (Connelly-GPM, Peerless Metal, Quebec Metal Powder, Johnson Matthey, Alfa Aesar), and types (nano-Fe^0 particles, iron grains, granular ZVI) (Das et al., 2017; Gibson et al., 2012; Liang et al., 2013; Olegario et al., 2010; Shi et al., 2015; Shrimpton et al., 2015; Tang et al., 2014; Yoon et al., 2011; Yoon et al., 2016; Zhang et al., 2005) have shown promise when compared to other reactive materials including pillared bentonite (Dong et al., 2016;

Li et al., 2015), organic matter (Gibson et al., 2012), transition metals (Tang et al., 2014), and iron (hydr)oxides (Balistrieri and Chao, 1990; Das et al., 2013; Hayes et al., 1987; Manceau and Charlet, 1994; Su and Suarez, 2000;).

Few studies (Gibson et al., 2012; Olegario et al., 2010; Tang et al., 2014; Yoon et al., 2011) have examined Se(VI) removal kinetics and mechanisms by ZVI under anoxic conditions. Moreover, none have employed Se(VI) concentrations typical of mine waters (Hendry et al., 2015; Lussier et al., 2003; Wellen et al., 2015) and evaluated the impacts of NO_3^- and SO_4^{2-} on Se removal. Recently, Das et al. (2017) evaluated Se(VI) removal rates and mechanisms by three commercially-available ZVI materials. These experiments were conducted under oxic conditions in the presence and absence of NO_3^- and SO_4^{2-} with an initial Se concentration of 1 mg L^{-1} (Das et al., 2017). Results demonstrated that, although effective Se(VI) removal can be achieved, the presence of SO_4^{2-} and NO_3^- was associated to decreased reaction rates and inhibited reduction (Das et al., 2017). However, ZVI is a strong reductant and it remains unclear what impact the development of anoxic conditions will have on Se(VI) removal (Gibson et al., 2012; Yoon et al., 2011).

This study examines the impact of SO_4^{2-} and NO_3^- on Se(VI) removal rates and mechanisms by ZVI under anoxic conditions. Laboratory batch experiments assess Se(VI) removal rates in the presence and absence of SO_4^{2-} and NO_3^- using a commercially-available ZVI source selected based upon Das et al. (2017). Associated solid-phase analyses examine Se speciation and ZVI corrosion products to further constrain reaction mechanisms. Overall, this study offers new insights into factors influencing ZVI treatment of Se contaminated mine waters. Results are also relevant to Se removal from water impacted by other anthropogenic activities.

MATERIALS AND METHODS

Batch experiments were performed to evaluate Se(VI) removal rates and mechanisms under anoxic conditions. These experiments utilized dissolved Se(VI) concentrations characteristic of waters contaminated by mining and metallurgical operations (Hendry et al., 2015; Lemly, 2004; Su and Puls, 2004; Suzuki et al., 2012; Wellen et al., 2015), and considered the impacts of SO_4^{2-} and NO_3^- on Se removal.

Input solutions. Four batch experiments were conducted using input solutions containing 5 mg L^{-1} Se(VI) in the presence or absence of 1800 mg L^{-1} SO_4^{2-} and 15 mg L^{-1} NO_3^- (as N). Input solutions used for these batches were as follows: (B1) Se(VI); (B2) Se(VI) + SO_4^{2-}; (B3) Se(VI) + NO_3^-; and (B4) Se(VI) + SO_4^{2-} + NO_3^-. These solutions were prepared in an anoxic chamber (≤ 5% $H_{2(g)}$, balance $N_{2(g)}$) by dissolving (ACS grade and anhydrous) (g L^{-1}) Na_2SeO_4 (0.012), Na_2SO_4 (3.24), and $NaNO_3$ (0.0753) in Type-1 ultra-pure (18.2 MΩ·cm) water that was first purged with high-purity $N_{2(g)}$ for 24 h.

Zero-Valent Iron. Ground-cast Fe aggregate (8/50) from Peerless Metal Powders and Abbrasives Co. (Detroit, USA) was selected based on previous research (Das et al., 2017). According to the manufacturer, this ZVI material contained approximately 90% (w/w) Fe and 4% (w/w) C with traces of Mn, Si, and Cr. The surface area of this ZVI is low (2.3 m^2 g^{-1}) and the particle size ranges from 0.368 to 2.36 mm (Das et al., 2017). Das et al (2017) reported that the ZVI is mainly composed of Fe(0) with some iron oxides such as magnetite (Fe_3O_4) and wüstite (FeO).

Approximately 100 g of ZVI was sieved to isolate particle sizes ranging from 0.0625 to 0.25 mm (mesh 230-60, fine and very fine sand). This ZVI was then moved into the glovebox and allowed to degas for 24 h. All ZVI was acid washed and dried immediately in the glovebox

following the method in Shrimpton et al. (2015) with minor modifications to remove oxide coatings on the ZVI surfaces. Acid washing consisted of soaking the ZVI in 50 mL of 1 M hydrochloric acid (HCl) for 1.5 h (until bubbling ceased), with stirring every 15 min to ensure total reaction, followed by two more soakings for 1.5 and 5 h, respectively. Final rinsing was done with 50 mL of 1 M hydroxylamine hydrochloride ($NH_2OH.HCl$) followed by four rinses with ultra-pure water until the supernatant was clear. Acid-washed ZVI was then dried in the glovebox for 24 h.

Two g samples ZVI were separated into 1-L beakers and stirred with 1 L of solution on a magnetic stir plate at 300 rpm during all experiments. The calibrated pH (VWR symphony) (using 4, 7, and 10 buffer solutions) and redox electrodes (Accumet) (checked using ORP electrode solutions) were immersed in the slurry and recordings taken at all sampling intervals (0.13 to 2 h for B1, 3 to 48 h for B2, 0.3 to 7 h for B3, and 6 to 192 h for B4). Temperature and O_2 concentrations were also measured at the same intervals in the glovebox. At each sampling interval, 11 mL of sample were removed using a syringe and filtered through 0.2-µm PES filters into two 1-mL vials for ion chromatography (IC) and spectrophotometric analyses and one 15-mL vial for inductively coupled plasma–optical emission spectroscopy (ICP-OES) analysis. Anion concentrations (i.e., NO_3^-, NO_2^-, and SO_4^{2-}) were analyzed on non-acidified samples immediately after sample collection by IC (ICS2100, Dionex Corporation, USA). Other samples were immediately acidified with 2% trace-metal grade nitric acid (HNO_3) (Fisher Scientific) and allowed to react for 24 h prior to analysis for total Se concentrations by ICP-OES (SPECTROBLUE SOP, SPECTRO Analytical Instruments GmbH, Germany). Total ammonium (NH_4^+) analyses were conducted on samples from the B3 and B4 batches via spectrophotometric analyses (DR2800, Hach Chemical Co., USA) (Nessler method). After completion of the

experiments, the supernatant was poured off and the solids dried for 24 h before being sealed in glass vials for further analysis.

Solids analyses

Gently ground samples (<90 μm) of the un-reacted (sieved to <90 μm and washed) and reacted ZVI materials from all four batches (i.e., B1, B2, B3, B4) were analyzed via X-ray diffraction (XRD), Raman spectroscopy (RS), transmission electron microscopy (TEM), and Brunauer-Emmett-Teller (BET) surface area analyses for ZVI particle morphology and mineralogy. In addition, the ZVI samples collected at the termination of each batch experiment were analyzed via X-ray absorption near edge structure (XANES) spectroscopy for Se speciation on the ZVI surfaces.

XRD and Raman Spectroscopy. XRD and Raman spectroscopic analyses were conducted on five ground samples (sieved and washed as well as reacted samples from each of the four batches). X-ray diffraction analyses were performed on an X-ray diffractometer equipped with a Co X-ray tube (Empyrean, PANalytical B.V., Netherlands) using the method presented in Das et al. (2017). Briefly, unoriented ground samples were placed on a spinning reflection/transmission stage and scans collected from 10 to 80° (step size of 0.0167°) with a scan speed of 1° min^{-1}. Mineral phases of ZVI samples were identified by HighScore Plus (PANalytical B.V., Netherlands) and the ICDD database (International Centre for Diffraction Data, USA).

Raman spectroscopy used a Raman microscope (inVia Reflex, Renishaw plc, UK) following the method in Das et al. (2017) but with minor modifications. In brief, after internal calibration (Si standard; Raman shift 520 cm^{-1}), ~2 mg of a solid sample were mounted on a glass slide and viewed under the microscope (20X N PLAN). Once a suitable area was selected (achieved after several quick scans), samples were analyzed using a 785 nm laser (1200 lines mm^{-1} grating) with

1% laser power (0.1% in Das et al., 2017) and 10 s detector exposure time. A total of 32 spectral accumulations were collected for each sample to increase the signal to noise ratio.

TEM. Transmission electron microscopy (TEM) imaging was performed for one pre-treated and four reacted ZVI samples to identify the morphology of the ZVI before and after aging. In brief, a solution of suspended particles of each sample was created by addition of 70% ethanol. Once homogenized, approximately 3 µL of the suspension was dropped onto a 300 mesh formvar/carbon copper grid (Agar Scientific) and allowed to dry (1 h). Subsequently, the grids containing ZVI samples were viewed and imaged using a Hitachi HT7700 with an accelerating voltage of 80 kV.

Surface area. Reactive surface areas were analyzed for two ZVI samples (pristine-untreated and pretreated) via multi point BET-nitrogen isotherms (NOVA 2200*e*, Quantachrome Instruments, USA). After 24 h of degassing at 70 °C, 11-point BET surface areas were analyzed (atmospheric pressure) with a p/p_0 range of 0.05 to 0.35.

XAS. Selenium K-edge X-ray absorption spectroscopy (XAS) was performed on reacted ZVI samples (B1–B4) and reference compounds including $NaSeO_{4(s)}$, Se(IV) adsorbed onto ferrihydrite, $Se_{(s)}$, and $FeSe_{(s)}$. Both samples and reference compounds were gently ground using a mortar and pestle, and reference compounds were subsequently diluted in $BN_{(s)}$ to achieve a final Se content of 1% (w/w). The solids were then packed into 0.5-mm thick polytetrafluoroethylene holders and sealed between two layers of polyimide tape. All sample preparations were conducted in an anoxic chamber.

Prepared samples were transported to the Hard X-ray Micro-Analysis (HXMA) beamline (06ID-1) at the Canadian Light Source (Saskatoon, Canada). The HXMA beamline uses a 2 T superconducting wiggler and Re-coated mirrors for upstream and downstream beam collimating

and focussing, respectively. Monochromatization of the incident white beam used two Si(111) crystals. Higher harmonics were omitted by detuning the second crystal to 50% of beam intensity. Energy step size was 0.25 eV over the X-ray absorption near edge structure (XANES) region and 0.05 $Å^{-1}$ in *k*-space up to 9.2 *k* in the extended X-ray absorption fine structure (EXAFS) region.

Fluorescence spectra were collected for ZVI samples under ambient conditions using a 32-element solid state Ge detector (Canberra Industries Inc., USA). Aluminum foil, Soller slits, and an As filter were positioned between the samples and detector to optimize signal-to-noise ratio. Reference spectra were obtained in transmission mode using the first and second ionization chambers, which were positioned immediately upstream and downstream of the reference materials, respectively. Energy calibration utilized transmission spectra for $Se_{(s)}$ foil, which positioned between downstream of the reference compounds between the second and third ionization chambers. Triplicate spectra were obtained for all samples, whereas duplicate spectra were collected for reference materials.

The ATHENA module of the XAS software package Demeter (v.0.9.24) (Ravel and Newville, 2005) was used data reduction and analysis. Energy calibration utilized the zero crossing of the second derivative of the reference $Se_{(s)}$ foil assumed to be 12658 eV. Replicate scans were then averaged before background removal and edge-step normalization. Linear combination fitting (LCF) was performed over the 50 eV region from 12640 to 12690 eV. Goodness of the fit was assessed using R-factors, where lower values are generally indicative of better fits.

Kinetic modeling. Selenium removal by ZVI for all four batches was modeled using a first-order reaction rate:

$$[A]_t = [A]_0 e^{-kt} + r \qquad (1)$$

where $[A]_t$ is the Se concentration (mg L^{-1}) during the reaction with ZVI at time t (h), $[A]_0$ is the Se concentration at the beginning of the ZVI reaction (mg L^{-1}), k is the rate constant (h^{-1}) of aqueous Se removal by ZVI, t is time (h), and r is the residual aqueous Se concentration (mg L^{-1}) at the end of the experiment. The R^2 values demonstrate the goodness of fit to experimental results, values approaching unity generally signifying better fits.

RESULTS AND DISCUSSION

Selenium removal rates. Selenium(VI) removal occurred rapidly in the absence of SO_4^{2-} and NO_3^- (B1) with 90% of the dissolved Se(VI) removed from solution within 1.5 h (Fig. 1). In contrast, 90% Se(VI) removal was achieved after approximately 3 h with NO_3^- (B3), 33 h with SO_4^{2-} added (B2), and 40 h in the presence of both SO_4^{2-} and NO_3^- (B4). Despite differences in rates among batches, Se(VI) removal followed first-order kinetics with R^2 values ranging from 0.96 to 0.99. The rate constant for Se(VI) removal without SO_4^{2-} and NO_3^- (B1) was 3.22 h^{-1}. The rate constant decreased to 0.99 h^{-1} with NO_3^- added (B3). Rate constants for Se(VI) removal with SO_4^{2-} added were 0.04 h^{-1} (B2) and 0.05 h^{-1} with SO_4^{2-} and NO_3^- (B4). The rate constants, which decreased by 65 to 80 times, demonstrate that SO_4^{2-} concentrations typical of mine wasters strongly inhibits Se(VI) removal under anoxic conditions. Reaction rates decreased by approximately three times in the presence of NO_3^-, suggesting this anion had a lesser impact on Se(VI) removal. This discrepancy in the impact of SO_4^{2-} and NO_3^- on Se(VI) removal may be associated to the large concentration difference between these anions; however, these concentrations are consistent with concentrations reported for mine waters (Hendry et al., 2015; Lussier et al., 2003; Wellen et al., 2015).

Das et al. (2017) conducted Se(VI) removal experiments using the same ZVI material (not washed or sieved) and equivalent SO_4^{2-} and NO_3^- concentrations, but under oxic conditions with

lower initial Se(VI) concentrations (1 mg L^{-1}) (Fig. S1). In the absence of both SO_4^{2-} and NO_3^- (B1), the anoxic Se(VI) removal rate (3.22 h^{-1}) was approximately 2.5 times greater than the corresponding oxic rate (1.30 h^{-1}) (Table 1, S1). Similarly, the rate constant for Se(VI) removal in the presence of NO_3^- (B3) under anoxic conditions (0.99 h^{-1}) was nearly double that for oxic conditions (0.53 h^{-1}). In contrast, the Se(VI) removal rate constant in the presence of SO_4^{2-} was similar under both oxic or anoxic conditions, at 0.07 or 0.03 h^{-1} for oxic and 0.04 or 0.05 h^{-1} for anoxic batches B2 (SO_4^{2-}) and B4 (NO_3^- + SO_4^{2-}), respectively (Table 1, S1). These results suggest that NO_3^- decreases the rate of Se(VI) removal but the effect of SO_4^{2-} is greater. Removal rates of Se(VI) by NO_3^- or SO_4^{2-} is described in the literature and termed passivation or poisoning of the ZVI surfaces (Reinsch et al., 2010; Zhang et al., 2005). The ultimate effect of passivation is to decrease the efficiency of Se(VI) removal by ZVI. It is proposed that NO_3^- can act as oxidants and thus oxidize the ZVI surface, which results in the formation of an Fe (hydr)oxide layer (Reinsch et al., 2010). Due to the formation of this protective oxide layer on the ZVI surface, the rate of Se(VI) reduction slows compared to pristine conditions. On the other hand, retardation of Se(VI) removal by ZVI can be attributed to by the similarities in the chemical properties of Se(VI) and SO_4^{2-} (Zhang et al., 2005). Owing to their similarities, SO_4^{2-} is possibly competing with Se(VI) for the surface sites on the ZVI surfaces (due to much higher concentrations of SO_4^{2-} with respect to Se(VI)) and thus lowering the adsorption of Se(VI) and consequently, lowering the rate of removal process (Zhang et al., 2005). Although Se(VI) removal rates are presented in the literature for a range of ZVI materials and varied porewater conditions, they can be described using simple first-order or pseudo first-order kinetics (Das et al., 2017; Liang et al., 2015; Olegario et al., 2010; Shrimpton et al., 2015; Yoon et al., 2011; Zhang et al., 2005). This observation is consistent with the current study.

pH, Eh and dissolved Fe. Initial pH ranged from 6.1 to 6.4 for all systems (B1, B2 and B4) except for the NO_3^--rich system (B3) which was measured at 8.4. Despite this discrepancy, the pH of all batches rapidly increased to ~8.4-9.0 after the addition of the ZVI and increased consistently for all four batches during aging. The final pH was 8.38, 9.13, 9.55, and 9.91 after the B1, B2, B3, and B4 batches were aged for 2, 48, 7, and 192 h, respectively (Fig. S2). The sorption envelope for both Se(IV) and Se(VI) decreases rapidly as pH increases from ~7 to ~9 (Rovira et al., 2008). This probably indicates that sorption is, perhaps, less important over time as ZVI corrosion proceeds and pH increases. This could have implications for B3 if the majority of Se removal occurred before the pH had increased to >8.

The increases in pH with time were inversely correlated with decreasing Eh values (Fig. S3) that occurred rapidly after the addition of ZVI to a value of -189, -443, -423, and -460 mV at the end of the experiments for B1, B2, B3, and B4 respectively. The progressive increase in pH and decrease in Eh can be explained by the following reaction:

$$Fe_{(s)} + 2H_2O_{(l)} \rightarrow Fe^{2+} + H_{2(g)} + 2OH^- \quad (2)$$

where Fe(0) corrosion (in the presence of water) results in the formation of H_2 and OH^- (Gibson et al., 2012; Liu et al., 2017; Shrimpton et al., 2015). The formation of OH^- and H_2 will result in an increase in the pH and decrease in the Eh in the systems tested. The reaction described in equation (1) also results in the production of aqueous Fe^{2+}. The total dissolved Fe content ranged from 0.02 (B1) to 3.8 mg L^{-1} (B4) during the experiments (Fig. S4).

Nitrate and sulfate concentrations. Decreasing NO_3-N concentrations were observed in both the B3 (NO_3^-) and B4 (NO_3^-+SO_4^{2-}) batches during the experiments. The NO_3-N concentrations decreased slightly from 13.1 to 11.5 mg L^{-1} during the 7 h reaction time for the B3 batch (Fig. 2a). The lack of any decrease of NO_3-N is attributed to the short reaction time. In

contrast, oxic batch test results conducted over a longer time period (32 h) exhibited a decrease in NO_3-N from 15.3 to 11.7 mg L^{-1}. These data for the oxic B3 batch (Das et al., 2017) followed a near linear trend. The B4 batch (NO_3^-+ SO_4^{2-}) showed a loss of NO_3-N from 11.4 to 8.74 mg L^{-1} over 192 h of reaction time, which followed a linear trend after about 96 h of induction time (Fig. 2b). These results suggest NO_3-N reduction is not a spontaneous process under anoxic conditions; in contrast, oxic data presented in Das et al. (2017) exhibit a more acute loss of NO_3-N (14.1 to 6.40 mg L^{-1}) over 194 h of reaction time. Unlike the anoxic dataset, the oxic batch showed no delay in the induction time and followed a linear decrease with time (Fig. 2b).

Note that a linear increase in NH_4^+-N concentrations was observed for the B4 batch under anoxic conditions with a simultaneous linear decrease in NO_3-N over time (Fig. 2b). In contrast, an increase and a subsequent decrease in NH_4^+-N concentrations was observed for oxic batch experiments (Das et al., 2017). The decrease in NH_4^+-N concentrations is attributed to the adsorption of NH_4^+ onto the ZVI surfaces under oxic conditions. However, this trend is not observed under anoxic conditions. The concentrations of nitrite (NO_2^--N) remained low throughout the experiments (B3 and B4), ranging from 0.0 to 0.4 and 0.0 to 0.6 mg L^{-1}, respectively, and thus does not appreciably contribute to N mass balance in the aqueous phase. Overall, this suggests that NO_3^- reduction might not be a favorable pathway under the anoxic conditions tested.

The results of this study are consistent with previous studies, suggesting that this subtle loss of NO_3^- in anoxic batches and subsequent production of NH_4^+ occurs during NO_3^- reduction by ZVI (Cheng et al., 1997; Choe et al., 2004; Su and Puls, 2004; Suzuki et al., 2012); via:

$$4\ Fe^0 + NO_3^- + 7\ H_2O \rightarrow 4\ Fe^{2+} + NH_4^+ + 10\ OH^- \qquad (3)$$

In contrast to NO_3^-, the SO_4^{2-} concentrations for both B2 and B4 show no trend with time (Fig. S5) and remain consistent, with initial concentrations (~1800 mg L^{-1}) maintained throughout

the experiments. This indicates that SO_4^{2-} does not undergo any reduction or adsorption during Se(VI) removal by ZVI.

Solid-phase Se speciation. The LCF results of Se K-edge XANES spectra suggest that ZVI effectively reduced Se(VI) to elemental selenium for all batches (B1-B4) (Fig. 3; Table 2) irrespective of geochemical conditions tested. Specifically, LCF analyses of solids samples from batches B1, B2, B3, and B4 yielded ~71, ~74, ~80, and ~76% of Se(0) on the reacted solids, respectively (Fig. S6; Table 2). The LCF analyses also indicate that 10-13% of the Se in the solid phase samples is present as Se(IV) and a few percent as Se(-II) (highest for B1, 12.6%) (Table 2). Around 7-9% of Se remains as Se(VI) on the ZVI surfaces along with other Se species at the end of the experiments. These findings show that although both NO_3^- and SO_4^{2-} limit the rate of Se(VI) removal, the concentration of these anions does not play an important role in controlling the primary reduction products. However, the formation of Se(-II) appears to be more limited in the NO_3^--rich batch (1.8%) (B3) compared to SO_4^{2-}- (4.7%) (B2) and $NO_3^- + SO_4^{2-}$-rich batches (4.8%) (B1) (Table 2).

In contrast to the current results, Se speciation includes both Se(IV) and Se(0) following removal by ZVI under oxic conditions (Table 2) (Das et al., 2017). Further, the oxic test results do not indicate the presence of any Se(-II) during the reduction process whereas up to 13% of the Se on the ZVI was present as Se(-II) for the anoxic experiments (Table 2) when both NO_3^- and SO_4^{2-} were absent.

Results of these S K-edge XANES analyses are consistent with previous results, which reported the presence of Se(IV), Se(0), and Se(-II) following Se(VI) removal by ZVI (Das et al., 2017; Liang et al., 2013; Olegario et al., 2010; Yoon et al., 2011). Overall, XANES analyses suggest that anoxic conditions provide more favorable pathway(s) to remove aqueous Se(VI) via

reduction to more reduced species such as Se(0) and Se(-II) compared to oxic conditions (Das et al., 2017).

ZVI surface characteristics. Transmission electron microscopic (TEM) images of sieved and washed ZVI (non-reacted) show the individual grain morphology is rounded to sub-rounded in nature with a thin rim-like structure (a darker rim compared to a lighter core) surrounding a single grain (Fig. S6a). Similar individual grain morphology was observed by Liu et al. (2017) after their anoxic batch experiments. These authors suggest the core is composed of Fe(0) and the thin rim of an Fe oxide coating. The reacted (B1-B4) ZVI grain morphology shows that the shape of the individual particle and rim-like structure did not change noticeably after aging in all four batches tested, irrespective of reaction times (Fig. S7b-e). Liu et al. (2017) also observed that ZVI shape remains similar after 72 h of aging and suggest the ZVI shape stays close to its pristine nature due to lower oxidation and corrosion rate of ZVI under anoxic versus oxic conditions.

Brunauer–Emmett–Teller (BET) surface area analyses show the untreated ZVI has a low surface area (2.3 $m^2\ g^{-1}$) that is consistent with measurements of 1.63 and 2.3 $m^2\ g^{-1}$ for PM reported in other studies (Das et al., 2017; Zhang et al., 2005). The surface area we determined for a sieved and acid washed sample (9.7 $m^2\ g^{-1}$) was greater than for an unwashed sample and is attributed to washing off low surface area oxide coatings (e.g., lepidocrocite and magnetite).

X-ray diffraction (XRD) scans indicate the ZVI sample (sieved and washed) consisted of Fe(0), minor magnetite [Fe_3O_4], and traces of lepidocrocite [γ-FeOOH] (Fig. 4). The XRD results also show the mineralogy of the ZVI surfaces did not change after aging in all four batches (Fe(0) remained the dominant Fe phase along with minor amounts of magnetite and lepidocrocite) (Fig. 4B1-B4). These data corroborate the TEM analyses that show the ZVI does not undergo significant alterations by the end of the testing periods.

Raman spectral analyses revealed magnetite (~670 cm^{-1}), lepidocrocite (232 and 372 cm^{-1}), and traces of goethite (~300 cm^{-1}) at ZVI surfaces from the reacted samples (Fig. 5). In addition to magnetite and lepidocrocite, carbon was also observed (~1315 and ~1585 cm^{-1}) in a non-reacted sample from this current study. These phases are consistent with previous Raman analyses reported by Das et al. (2017) for non-reacted ZVI surfaces (Fig. 5). Raman analyses on reacted samples also indicate the ZVI mineralogy remained similar in all four batches (bands of both magnetite and lepidocrocite are visible along with carbon) (Fig. 5B1-B4) and corroborate both TEM and XRD analyses.

Overall, solids analyses show that the ZVI does not undergo measurable transformation or oxidation during anoxic aging. In terms of secondary mineralogy, results obtained from XRD and Raman analyses are consistent with the literature. Dominant secondary mineral phases magnetite, lepidocrocite, and goethite have been reported during aging of ZVI under both oxic and anoxic conditions (Das et al., 2017; Gunawardana et al., 2012; Liu et al., 2017; Olegario et al., 2010; Yoon et al., 2011). Although trace amounts of other iron minerals including ferrihydrite, hematite, schwertmannite, mikasaite, and vivianite are reported in the literature (Gunawardana et al., 2012; Petr et al., 2012; Reinsch et al., 2010), these were not identified in the current study; this is attributed to dissimilar geochemical conditions (oxic vs. anoxic). Das et al. (2017) observed wustite [FeO] in an unreacted ZVI (PM) sample. Our inability to observe this mineral in the current study is attributed to its probable removal during pre-treatment (sieving and acid washing).

CONCLUSIONS

This study assessed the reduction and subsequent removal of Se(VI) by ZVI under anoxic conditions in the presence and absence of SO_4^{2-} and NO_3^-. Solid samples were collected for Se speciation and secondary mineralogy after completion of each experiment. Results show that

Se(VI) removal is a fast process, with about 90% of Se(VI) removed within ~1.5 h in the absence of SO_4^{2-} and NO_3^-. The presence of SO_4^{2-} and NO_3^- in the test waters reduces the rates of Se(VI) removal by factors of ~80 and 3.25, respectively. The decrease in the rates of Se(VI) removal under NO_3^- dominated system was attributed to oxidation and passivation of the ZVI surface that hindered the reduction process. On the contrary, SO_4^{2-} can compete for the surface sites with Se(VI), and thus reduce adsorption of Se(VI) and in the process slowdown the reduction rate. Despite differences in reaction rates among batches, Se(VI) removal as consistently fit using a first-order kinetic model. Additionally, Se(VI) removal rates in all anoxic batch experiments conducted here are faster compared to the similar tests under oxic conditions reported by Das et al. (2017). However, Se(VI) removal rates were similar in the presence of SO_4^{2-} under both oxic and anoxic conditions. During Se(VI) removal process, the ZVI is partially oxidized to magnetite [Fe_3O_4] and, to a lesser extent, lepidocrocite [γ-FeOOH]. Overall, this study illustrates that ZVI can reduce more soluble Se(VI) to less soluble Se(IV) and insoluble Se(0) and Se(II) species under anoxic conditions.

ACKNOWLEDGMENTS

The authors acknowledge funding provided by the Natural Sciences and Engineering Research Council of Canada (NSERC) IRC program (MJH; Grant No. 184573) and Discovery Grant program (MBJL; Grant No. RGPIN-2014-06589). The authors also acknowledge the Canadian Light Source, whose operations are supported by the University of Saskatchewan, the Government of Saskatchewan, Western Economic Diversification Canada, the National Research Council Canada, and the Canadian Institutes of Health Research. The authors also thank Ms. Fina Nelson and Dr. Jared Robertson for assistance provided during batch and XAS experiments, respectively.

Supplementary Information

Comparison of measured aqueous Se(VI) concentrations (C/C_0) with time for B1, B2, B3, and B4 batches under anoxic and oxic (Das et al., 2017) conditions. pH, Eh, Fe(T), and sulfate concentrations of respective batches along with TEM images of un-reacted and reacted ZVI surfaces. Detailed linear combination fitting of Se K-edge XANES spectra, absorption energy values for the Se K-edge of E_0 (first inflection point), and the most intense peak (white line) for Se reference standards (seven figures and two tables).

REFERENCES

Bailey RT, Gates TK, Halvorson AD (2013) Simulating variably-saturated reactive transport of selenium and nitrogen in agricultural groundwater systems. J Contam Hydrol 149:27-45.

Balistrieri LS, Chao TT (1990) Adsorption of selenium by amorphous iron oxyhydroxide and manganese dioxide. Geochim Cosmochim Acta 54:739-751.

Cheng IF, Muftikian R, Fernando Q, Korte N (1997) Reduction of nitrate to ammonia by zero-valent iron. Chemosphere 35:2689-2695.

Choe S, Liljestrand HM, Khim J (2004) Nitrate reduction by zero-valent iron under different pH regimes. Appl Geochem 19:335-342.

Das S, Hendry MJ, Essilfie-Dughan J (2013) Adsorption of selenite onto ferrihydrite, goethite, and lepidocrocite under neutral pH conditions. Appl Geochem 28:185-193.

Das S, Lindsay MBJ, Essilfie-Dughan J, Hendry MJ (2017) Dissolved selenium(VI) removal by zero-valent iron under oxic conditions: influence of sulfate and nitrate. ACS Omega 2:1513-1522.

Diehl SF, Goldhaber M, Koenig AE, Ruppert L (2012) Distribution of arsenic, selenium, and other trace elements in high pyrite Appalachian coals: evidence for multiple episodes of pyrite formation. Int J Coal Geol 94:238-249.

Dong H, Chen Y, Sheng G, Li J, Cao J, Li Z, Li Y (2016) The roles of a pillared bentonite on enhancing Se(VI) removal by ZVI and the influence of co-existing solutes in groundwater. J Hazard Mater 304:306-312.

Essilfie-Dughan J, Hendry MJ, Dynes J, Hu Y, Biswas A, Barbour SL, Day S (2017) Geochemical and mineralogical characterization of sulfur and iron in coal waste rock, Elk Valley, British Columbia, Canada. Sci Total Environ 586:753-769.

Gibson BD, Blowes DW, Lindsay MBJ, Ptacek CJ (2012) Mechanistic investigations of Se(VI) treatment in anoxic groundwater using granular iron and organic carbon. J Hazard Mater 241-242: 92-100.

Gunawardana B, Singhal N, Swedlund P (2012) Dechlorination of pentachlorophenol by zero valent iron and bimetals: effect of surface characteristics and bimetal preparation procedure. Proc Int Conf Soils Sed Wat Energ 17:68-81.

Hayes KF, Roe AL, Brown Jr GE, Hodgson KO, Leckie JO, Parks GA (1987) In situ x-ray absorption study of surface complexes: selenium oxyanions on α-FeOOH. Science 238:783-786.

Hendry MJ, Biswas A, Essilfie-Dughan J, Chen N, Day SJ, Barbour SL (2015) Reservoirs of selenium in coal waste rock: Elk Valley, British Columbia, Canada. Environ Sci Technol 49:8228-8236.

Hendry MJ, Wassenaar LI, Barbour SL, Schabert MS, Birkham TK, Fedec T, Schmeling EE (2018) Assessing the fate of explosives derived nitrate in mine waste rock dumps using the stable isotopes of oxygen and nitrogen. Sci Total Environ 640-641:127-137.

Kang Y, Inoue N, Rashid MM, Sakurai K (2002) Fixation of soluble selenium in contaminated soil by amorphous iron (hydr)oxide. Environ Sci 15:173-182.

Kolker A (2012) Minor element distribution in iron disulfides in coal: A geochemical review. Int J Coal Geol 94:32−43.

Lemly AD (2004) Aquatic selenium pollution is a global environmental safety issue. Ecotox Environ Safe 59:44-56.

Li Y, Cheng W, Sheng G, Li J, Dong H (2015) Synergetic effect of a pillared bentonite support on SE(VI) removal by nanoscale zero valent iron. Appl Catal B 174-175:329-335.

Liang L, Guan X, Huang Y, Ma J, Sun X, Qiao J, Zhou G (2015) Efficient selenate removal by zero-valent iron in the presence of weak magnetic field. Sep Purif Technol 156:1064-1072.

Liang L, Yang W, Guan X, Li J, Xu Z, Wu J, Huang Y, Zhang X (2013) Kinetics and mechanisms of pH-dependent selenite removal by zero valent iron. Water Res 47:5846–5855.

Lindsay MBJ, Moncur MC, Bain JG, Jambor JL, Ptacek CJ, Blowes DW (2015) Geochemical and mineralogical aspects of sulfide mine tailings. Appl Geochem 57:157–177.

Liu A, Liu J, Han J, Zhang W-X (2017) Evolution of nanoscale zero-valent iron (nZVI) in water: microscopic and spectroscopic evidence on the formation of nano- and micro-structured iron oxides. J Hazard Mater 322:129-135.

Lussier C, Veiga V, Baldwin S (2003) The geochemistry of selenium associated with coal waste in the Elk River Valley, Canada. Environ Geol 44:905-913.

Mahmood FN, Barbour SL, Kennedy C, Hendry MJ (2017) Nirate release from coal waste rock dumps in Elk Valley, British Columbia. Sci Total Environ 605-606:915-928.

Manceau A, Charlet L (1994) The mechanism of selenite adsorption on goethite and hydrous ferric oxide. J Colloid Interface Sci 168:87-93.

Masscheleyn PH, Delaune RD, William HP (1990) Transformations of selenium as affected by sediment oxidation-reduction potential and pH. Environ Sci Technol 24:91-96.

Olegario JT, Yee N, Miller M (2010) Reduction of Se(VI) to Se(-II) by zerovalent iron nanoparticle suspensions. J Nanopart Res 12:2057-2068.

Palmer MA, Bernhardt ES, Schlesinger WH, Eshleman KN, Foufoula-Georgiou E, Hendryx MS, Lemly AD, Likens GE, Loucks OL, Power ME, White PS, Wilcock PR (2010) Mountaintop mining consequenses. Science 327:149-149.

Petr M, Šišková K, Machala L, Kašlík J, Šafářová K, Zbořil R (2012) Laser-induced transformations of zero-valent iron particles. AIP Conf Proc 47-5.

Ravel B, Newville M (2005) ATHENA, ARTEMIS, HEPHAESTUS: data analysis for X-ray absorption spectroscopy using IFEFFIT. J Synchrotron Rad 12:537-541.

Reinsch BC, Forsberg B, Penn RL, Kim CS, Lowry GV (2010) Chemical transformations during aging of zerovalent iron nanoparticles in the presence of common groundwater dissolved constituents. Environ Sci Technol 44:3455-3461.

Riley KW, French DH, Lambropoulos NA, Farrell OP, Wood RA, Huggins FE (2007) Origin and occurrence of selenium in some Australian coals. Int J Coal Geol 72:72-80.

Rovira M, Giménez J, Martínez M, Martínez-Llado X, de Pablo J, Martí V, Duro L (2008) Sorption of selenium(IV) and selenium(VI) onto natural iron oxides: goethite and hematite. J Hazard Mater 150:279-284.

Sasaki K, Blowes DW, Ptacek CJ (2008) Spectroscopic study of precipitates formed during removal of selenium from mine drainage spiked with selenate using permeable reactive materials. Geochem J 42:283-294.

Scheinost AC, Charlet L (2008) Selenite reduction by mackinawite, magnetite and siderite: XAS characterization of nanosized redox products. Environ Sci Technol 42:1984-1989.

Shi Z, Fan D, Johnson RL, Tratnyek PG, Nurmi JT, Wu Y, Williams KH (2015) Methods for characterizing the fate and effects of nano zerovalent iron during groundwater remediation. J Contam. Hydrol 181:17-35.

Shrimpton HK, Blowes DW, Ptacek CJ (2015) Fractionation of selenium during selenite reduction by granular zerovalent iron. Environ Sci Technol 49:11688-11696.

Su C, Puls RW (2004) Nitrate reduction by zerovalent iron: effects of formate, oxalate, citrate, chloride, sulfate, borate, and phosphate. Environ Sci Technol 38:2715-2720.

Su C, Suarez DL (2000) Selenate and selenite sorption on iron oxides: an infrared and electrophoretic study. Soil Sci Soc Am J 64:101-111.

Suzuki T, Moribe M, Oyama Y, Niinae M (2012) Mechanism of nitrate reduction by zero-valent iron: equilibrium and kinetics studies. Chem Eng 183:271-277.

Tang C, Huang YH, Zeng H, Zhang Z (2014) Reductive removal of selenate by zero-valent iron: the roles of aqueous Fe^{2+} and corrosion products, and selenate removal mechanism. Water Res 67: 166-174.

Tokunaga TK, Brown GE, Pickering IJ, Sutton SR, Bait S (1997) Selenium redox reactions and transport between ponded waters and sediments. Environ Sci Technol 31:1419-1425.

Wellen CC, Shatilla NJ, Carey SK (2015) Regional scale selenium loading associated with surface coal mining, Elk Valley, British Columbia, Canada. Sci Total Environ 532:791-802.

Yigit NO, Tozum S (2012) Removal of selenium species from waters using various surface-modified natural particles and waste materials. Clean-Soil Air Wat 0:1-11.

Yoon I-H, Kim K-W, Bang S, Kim MG (2011) Reduction and adsorption mechanisms of selenite by zero-valent iron and related corrosion. Appl Catal B 104:185-192.

Yoon I-H, Bang S, Kim K-W, Kim MG, Park SY, Choi W-K (2016) Selenate removal by zero-valent iron in oxic condition: the role of Fe(II) and selenate removal mechanism. Environ Sci Pollut Res 23:1081−1090.

Yudovich YE, Ketris MP (2006) Selenium in coal: a review. Coal Geol 67:112-126.

Zhang P, Sparks DL (1990) Kinetics of selenate and selenite adsorption/desorption at the goethite/water interface. Environ Sci Technol 24:1848-1856.

Zhang Y, Wang J, Amrhein C, Frankenberger Jr WT (2005) Removal of selenate from water by zerovalent iron. J Environ Qual 34:487-495.

Ziemkiewicz PF, O'Neal M, Lovett RJ (2011) Selenium leaching kinetics and in situ control. Mine Water Environ 30:141-150.

Figure captions

Figure 1. Measured (symbols) and modeled (lines) aqueous Se(VI) concentrations (C/C_0) with time for B1, B2, B3, and B4 batch tests.

Figure 2: Nitrate (as N) and ammonium (as N) concentrations with time for the (a) B3 (NO_3^-) and (b) B4 ($NO_3^- + SO_4^{2-}$) batches. Solid brown circles and solid blue squares represent nitrate from anoxic and oxic experiments, respectively, and the hollow brown circles and hollow blue squares represent ammonium for anoxic and oxic experiments, respectively. The oxic batch experimental data are from Das et al. (2017).

Figure 3: XANES (Se K-edge) spectra of reacted ZVI for batches B1, B2, B3, and B4 along with the reference compounds selenate (+VI), selenite (+IV), elemental selenium (Se 0), and selenide (Se-II). The K-edge reference energies (Table S2) for the respective oxidation states are presented as vertical dashed lines.

Figure 4. X-ray diffraction scans of non-reacted and reacted ZVI. The abbreviations Lp and Mt indicate lepidocrocite and magnetite, respectively.

Figure 5. Raman spectroscopic analyses of non-reacted and reacted ZVI. The abbreviations C, Gt, Lp, and Mt indicate carbon, goethite, lepidocrocite, and magnetite, respectively.

Tables

Table 1. Rate of Se(VI) removal and parameters used for kinetic modeling for B1 (5 mg L^{-1} Se), B2 (5 mg L^{-1} Se + 1800 mg L^{-1} SO_4^{2-}), B3 (5 mg L^{-1} Se + 12 mg L^{-1} NO_3–N), and B4 (5 mg L^{-1} Se + 1800 mg L^{-1} SO_4^{2-} + 12 mg L^{-1} NO_3–N) batches under anoxic test conditions. $[A]_0$ represents initial Se(VI) concentrations, r is the residual Se(VI) concentration, and k is the rate constant of each reaction. The R^2 of each test represents the goodness of fit.

Batch	ZVI	$[A]_0$ (mg L^{-1})	r (mg L^{-1})	k (h^{-1})	R^2
B1	anoxic	0.86 (±0.05)	0.09 (±0.02)	3.22 (±0.38)	0.97 (±0.05)
B2	anoxic	1.28 (±0.05)	-0.25 (±0.05)	0.04 (±0.00)	0.99 (±0.03)
B3	anoxic	0.88 (±0.01)	0.02 (±0.03)	0.99 (±0.14)	0.96 (±0.06)
B4	anoxic	1.04 (±0.03)	0.00 (±0.00)	0.05 (±0.00)	0.99 (±0.02)

Table 2. Linear combination fitting of Se K-edge XANES spectra for reacted ZVI from B1 (1 mg L^{-1} Se), B2 (1 mg L^{-1} Se + 1800 mg L^{-1} SO_4^{2-}), B3 (1 mg L^{-1} Se + 15 mg L^{-1} NO_3-N), and B4 (1 mg L^{-1} Se + 1800 mg L^{-1} SO_4^{2-} + 15 mg L^{-1} NO_3–N). The oxic data are from Das et al. (2017)

Batch	ZVI	Se(VI)	Se(IV)	Se(0)	Se (-II)	Total	R-factor
B1	anoxic	6.7 (±0.2)	10.7 (±0.2)	70.6 (±0.5)	12.6 (±0.6)	99.8	0.0005
	oxic	4.8 (±0.8)	46.9 (±0.8)	52.3 (±2.1)	-	104.1	0.005
B2	anoxic	8.9 (±0.2)	12.1 (±0.2)	73.9 (±0.5)	4.7 (±0.7)	99.6	0.0006
	oxic	14.1(±1.0)	66.7 (±0.9)	25.0 (±2.5)	-	105.9	0.008
B3	anoxic	6.8 (±0.2)	11.7 (±0.2)	80.1 (±0.6)	1.8 (±0.7)	100.4	0.0007
	oxic	4.7 (±0.8)	49.7 (±0.8)	49.7 (±2.1)	-	104.1	0.005
B4	anoxic	6.5 (±0.2)	13.1 (±0.2)	75.7 (±0.5)	4.8 (±0.6)	100.0	0.0004
	oxic	11.7 (±1.1)	52.9 (±1.1)	42.6 (±2.5)	-	107.1	0.010

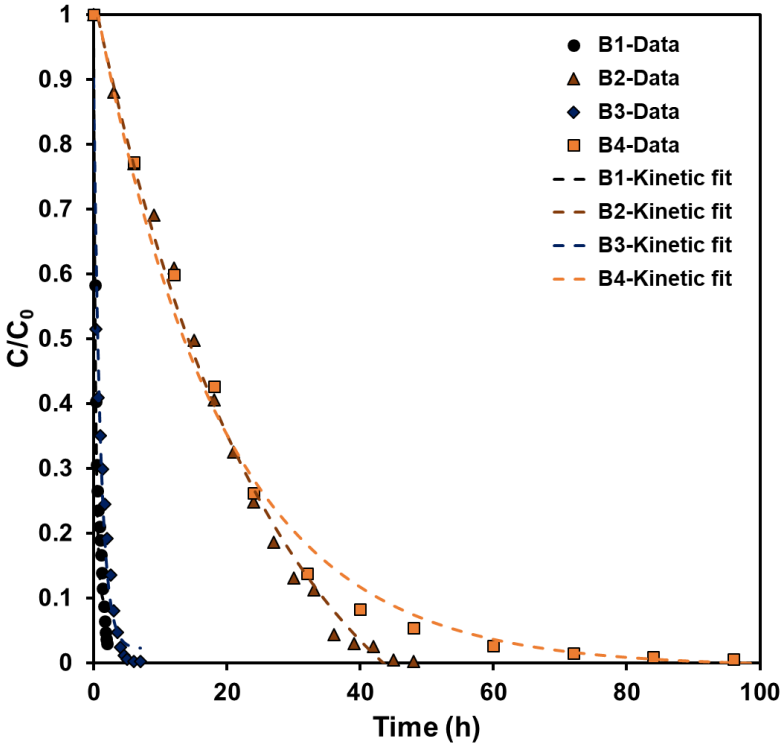

Figure 1

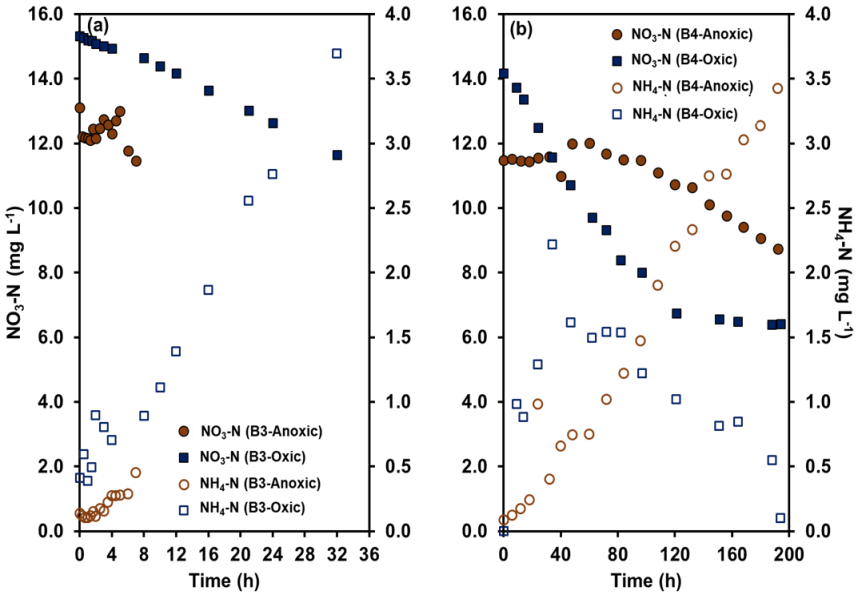

Figure 2

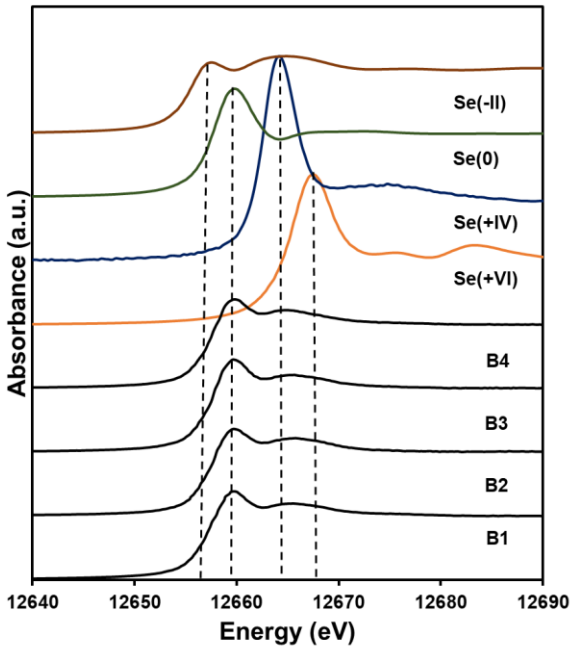

Figure 3

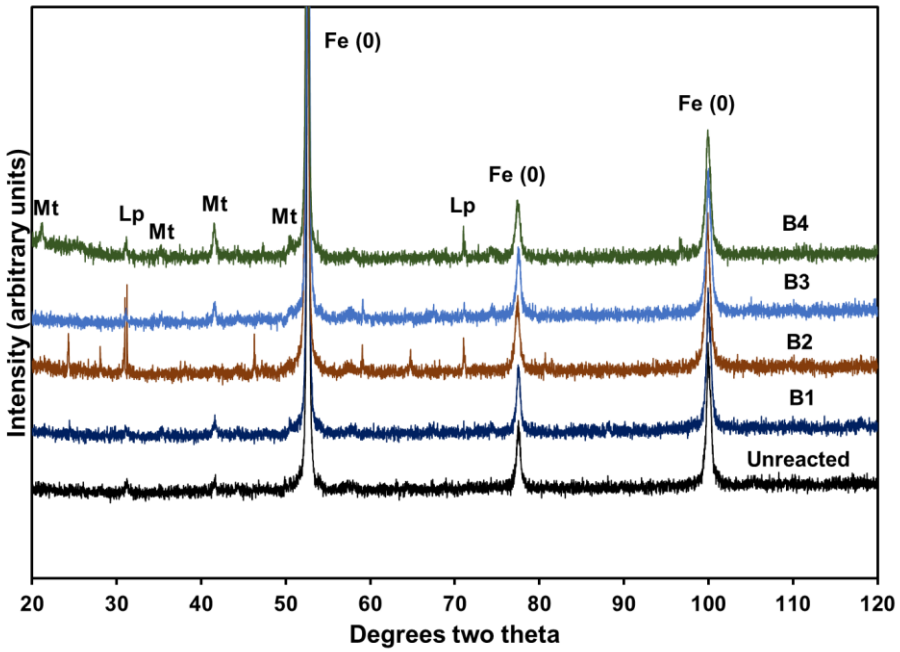

Figure 4

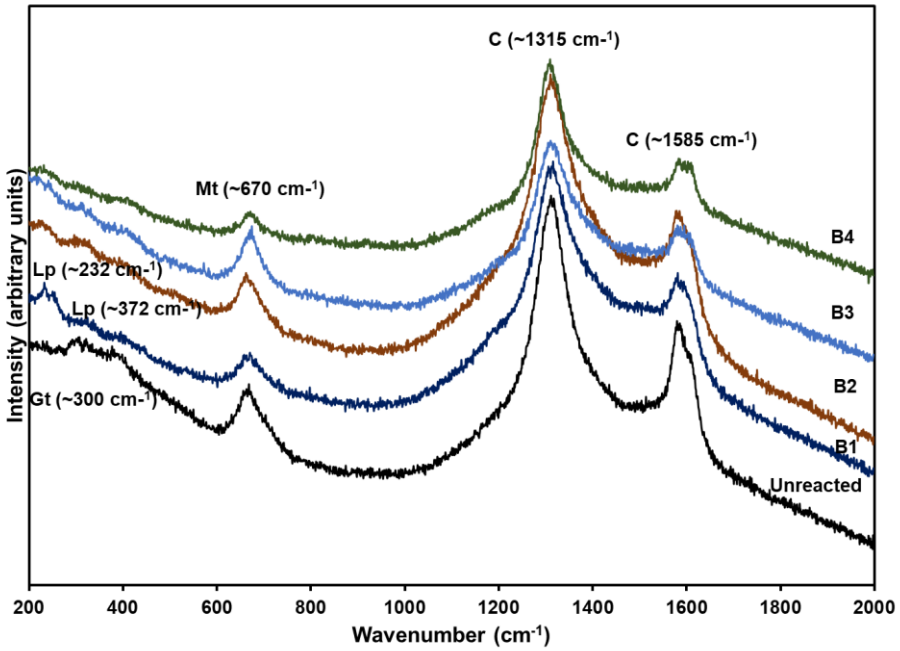
C (~1315 cm-1)
C (~1585 cm-1)
Mt (~670 cm-1)
Lp (~232 cm-1)
Lp (~372 cm-1)
Gt (~300 cm-1)
B4
B3
B2
B1
Unreacted
Intensity (arbitrary units)
200
400
600
800
1000
1200
1400
1600
1800
2000
Wavenumber (cm-1)

Figure 5